Applied Catalysis B: Environmental 220 (2018) 379–385

Contents lists available at ScienceDirect

Applied Catalysis B: Environmental

journal homepage: www.elsevier.com/locate/apcatb

2D heterostructure comprised of metallic 1T-MoS_2/Monolayer O-g-C_3N_4 towards efficient photocatalytic hydrogen evolution

Hui Xu[a,b], Jianjian Yi[a], Xiaojie She[a], Qin Liu[c], Li Song[c], Shuangming Chen[c], Yingchao Yang[b], Yanhua Song[d], Robert Vajtai[b], Jun Lou[b], Huaming Li[a,*], Shouqi Yuan[a], Jingjie Wu[e,**], Pulickel M. Ajayan[b,**]

[a] Institute for Energy Research, School of the Environment and Safety Engineering, Jiangsu University, Zhenjiang, 212013, PR China
[b] Department of Materials Science and NanoEngineering, Rice University, Houston, Texas 77005, USA
[c] National Synchrotron Radiation Laboratory, University of Science and Technology of China, Hefei, Anhui 230029, PR China
[d] School of Environmental and Chemical Engineering, Jiangsu University of Science and Technology, Zhenjiang 212003, PR China
[e] College of Engineering and Applied Science, University of Cincinnati, Cincinnati, OH 45221, USA

ABSTRACT

Efficient separation of hole-electron pair plays a crucial role in enhancing photocatalytic water splitting activity, which essentially requires a noble metal co-catalyst. Here we report that two-dimensional (2D) metallic 1T-MoS_2 can exceed the performance of noble metal like Pt as a co-catalyst in assisting the photocatalytic hydrogen evolution over 2D semiconductor such as oxygenated monolayer graphitic carbon nitride (O-g-C_3N_4). The abundance of intrinsic active site for hydrogen evolution reaction for 1T-MoS_2 partly contributes to the outstanding performance of 1T-MoS_2/O-g-C_3N_4 system. More importantly, the 2D heterostructure junction of 2D metals-2D semiconductor through van der Waals interaction minimizes the Schottky barrier, which in turn improves the charge transfer efficiency. The optimal 1T-MoS_2/O-g-C_3N_4 exhibited H_2 evolution rate as high as ~1841.72 μmol/g/h, an external quantum efficiency of ~7.11% at λ = 420 nm, and a super high TOF of 156.6 h^{-1}.

1. Introduction

The hydrogen evolution technology via photocatalytic water splitting in the presence of semiconductor is considered as a green and promising route to store solar energy in chemicals [1,2]. In order to achieve efficient photocatalytic hydrogen evolution reaction (HER) activity, co-catalysts, normally noble metals, are used to capture the photo-generated electrons on the surface of semiconductors. The noble metals usually possess large work function and low Fermi level position [3–5]. Therefore, it could much easily catch the photo-generated electrons to suppress the recombination of electron-hole (e-h) pairs. Platinum (Pt) as the most common noble metal with the lowest Fermi level position and zero-approaching Gibbs free energy of adsorbed H_{ads}, is the most effective co-catalyst for the photocatalytic HER [6–8]. Taking the hotspot g-C_3N_4 material as an example, photocatalytic water splitting activity of g-C_3N_4-based materials could only be significantly improved in the presence of Pt [9–11]. However, the expensiveness and scarcity of Pt and the other noble metals limit their wide applications. Therefore, it is essential to explore alternative noble-metal-free co-catalysts with earth abundance and high performance.

Two-dimensional (2D) transition metal dichalcogenides, especially MoS_2 existed in nature, have been considered as promising candidate to replace Pt for HER [12–14]. The MoS_2 material has two polymorphs: semiconducting phase (2H-MoS_2) with trigonal prismatic coordination and metallic phase (1T-MoS_2) with octahedral coordination [15]. Generally, 1T-MoS_2 shows better performance than 2H-MoS_2 in electrochemical HER, mainly because both the exposed edges and basal plane of the 1T-MoS_2 are catalytic active while only the edges are active in 2H phase [16–18]. 1T-MoS_2 as a co-catalyst has shown promising activity in TiO_2 and CdS-based photocatalysts [19,20]. The fast electron transfer rate from TiO_2/CdS to 1T-MoS_2 partly contributes to satisfactory photocatalytic HER in addition to abundant active sites. The common 3D metal-semiconductor junction has a large Schottky barrier (SB) which is difficult to tune because of the effect of strong Fermi level pinning (FLP). The 2D heterostructure composed of 2D metals-2D semiconductor through van der Waals interactions could decrease or

* Corresponding author at: Institute for Energy Research, School of the Environment and Safety Engineering, Jiangsu University, Zhenjiang, 212013, PR China.
** Corresponding authors.
E-mail addresses: lihm@ujs.edu.cn (H. Li), wu2jj@ucmail.uc.edu (J. Wu), ajayan@rice.edu (P.M. Ajayan).

http://dx.doi.org/10.1016/j.apcatb.2017.08.035
Received 14 June 2017; Received in revised form 7 August 2017; Accepted 11 August 2017
Available online 16 August 2017
0926-3373/ © 2017 Published by Elsevier B.V.

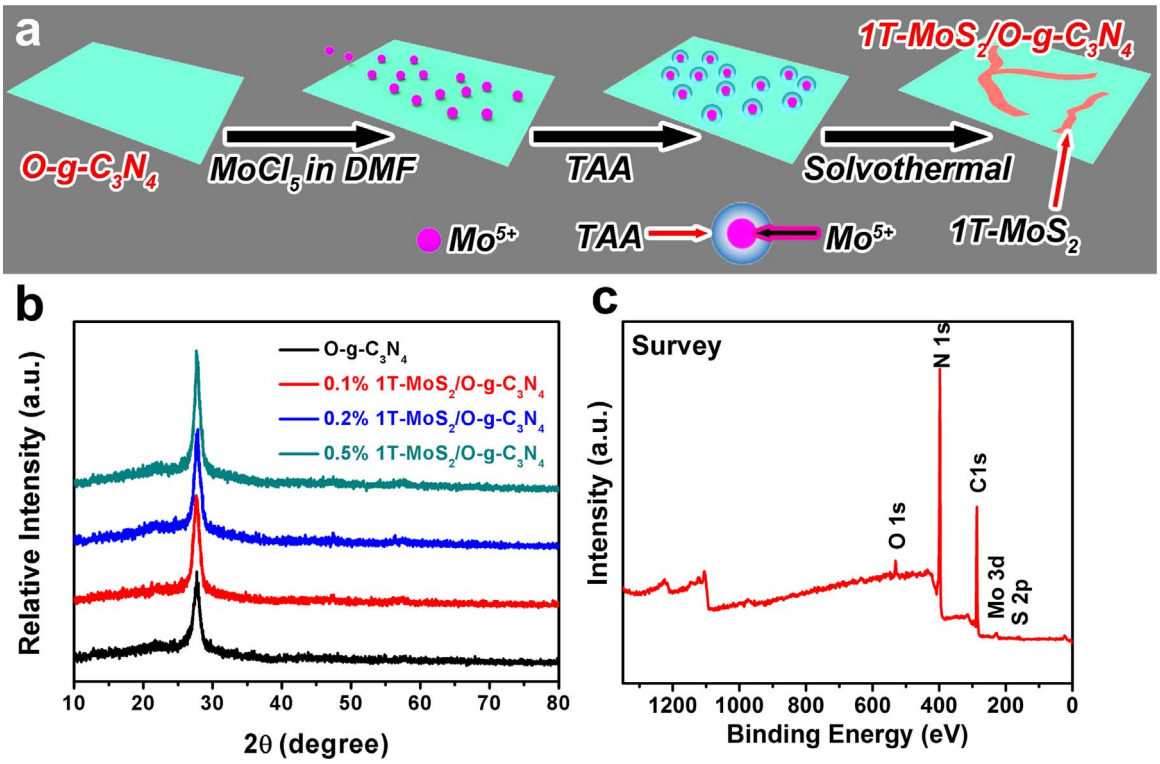

Fig. 1. (a) Schematic illustration of the synthetic process of 1T-MoS_2/O-g-C_3N_4. (b) XRD patterns and (c) XPS survey spectra of 0.2% 1T-MoS_2/O-g-C_3N_4.

even wipe out the SB due to weak FLP [21,22]. Therefore, the 2D heterostructure for example 2D 1T-MoS_2/2D g-C_3N_4 can further facilitate the electron transfer from semiconducting g-C_3N_4 to metallic 1T-MoS_2. In this work, we choose 2D oxygenated monolayer graphitic carbon nitride (O-g-C_3N_4) as a model semiconductor photocatalyst for the reasons below: (i) The suitable band structure for photocatalytic water splitting and visible light absorption; (ii) The environmental and economic friendly nature; (iii) Benefiting from the large specific area, O-g-C_3N_4 allows the robust anchoring of co-catalyst on its surface and effective charge transfer between two components, which could result in better performance and help us study the behavior of 1T-MoS_2 co-catalysts well [23].

Herein, we for the first time develop metallic 1T-MoS_2/O-g-C_3N_4 to form 2D heterostructure via the in-situ growth method. The 1T-MoS_2/O-g-C_3N_4 exhibits superior photocatalytic performance compared to single O-g-C_3N_4 and 2H-MoS_2/O-g-C_3N_4 sample. The H_2 evolution rate of 2D heterostructure of 1T-MoS_2/O-g-C_3N_4 is almost 24 times higher than that of Pt/O-g-C_3N_4 under the same co-catalyst loading of 0.1%. The 2D heterostructure of 1T-MoS_2/O-g-C_3N_4 with optimal 1T-MoS_2 loading of 0.2% exhibits the highest H_2 evolution rate (~1841.72 μmol/g/h). The external quantum efficiency (EQE) of 0.2% 1T-MoS_2/O-g-C_3N_4 achieves 7.11% at $\lambda = 420$ nm, which is the highest value in all g-C_3N_4-based system using Pt-free co-catalysts. The turnover frequency (TOF) is higher than all the reported Pt co-catalyzed g-C_3N_4, excepted for the using of single atom Pt.

2. Experimental section

2.1. Preparation of samples

1T-MoS_2/O-g-C_3N_4 2D heterostructure was fabricated by a in-situ growth method. The specific process is as follows: O-g-C_3N_4 (0.2 g) and $MoCl_5$ (0.0003 g, 0.0007 g and 0.0017 g, respectively) were dispersed in dimethylformamide (DMF). Then, 0.0450 g Thioacetamide (TAA) was added into the solution. After sonicating it for 30 min, the suspension was transferred to a Teflon-lined stainless steel autoclave (50 mL capacity), and then heated at 200°C for 24 h. When the autoclave cooled down to room temperature, the obtained samples were separated by centrifugation and washed with water and ethanol. Finally, they were freeze-dried for 24 h. The different molar ratios of 1T MoS_2 in the 2D heterostructures were denoted as 0.1%, 0.2% and 0.5%, respectively. O-g-C_3N_4 was prepared by the modified method according to the previous report (Fig. S1) [23], and the typical synthesis process was shown in Supplementary Information.

2H-MoS_2/O-g-C_3N_4 was prepared by heating 1T-MoS_2/O-g-C_3N_4 2D heterostructures under different calcination temperatures. 2H-MoS_2/O-g-C_3N_4(150 °C) and 2H-MoS_2/O-g-C_3N_4 (300 °C) samples were annealed at 150 °C and 300 °C in N_2 atmosphere, respectively.

2.2. Photoelectrochemical measurement

The 2D heterostructures were dispersed in ethylene glycol (EG) and ethanol (1: 1 by volume) through sonication, and the concentration of the sample was 1 mg/mL. 20 μL of the suspension was drop-casted onto an indiumtin oxide (ITO)-coated glass with an exposed area of 0.5 cm^2 (1 cm × 0.5 cm). Then, ITO-coated glasses were dried under the infrared lamp irradiation. The photocurrents of the samples were measured on the CHI660 B electrochemical analyzer (Shanghai Chenhua, China) under a 500 W Xe lamp irradiation. Ag/AgCl (saturated KCl solution), indiumtin oxide (ITO) glass and platinum (Pt) wire were used as the reference electrode, working electrode and the counter electrode, respectively. In the experiments, the bias potential of −0.2 V (*vs.* Ag/AgCl) was used. 0.1 M Na_2SO_4 solution was used as the electrolyte.

2.3. Photocatalytic H_2 evolution activity

Triethanolamine (TEOA) was used as the sacrificial agent of the photogenerated holes. 0.01 g of the samples were added to 100 mL TEOA/H_2O (1:9 by volume). Then, the suspension was homogenized through sonication. Before the light irradiation, the suspension was fully degassed to remove air. The light-irradiation was carried out by using a 300 W Xe lamp (PLS-SXE 300C (BF), PerfectLight, Beijing) with

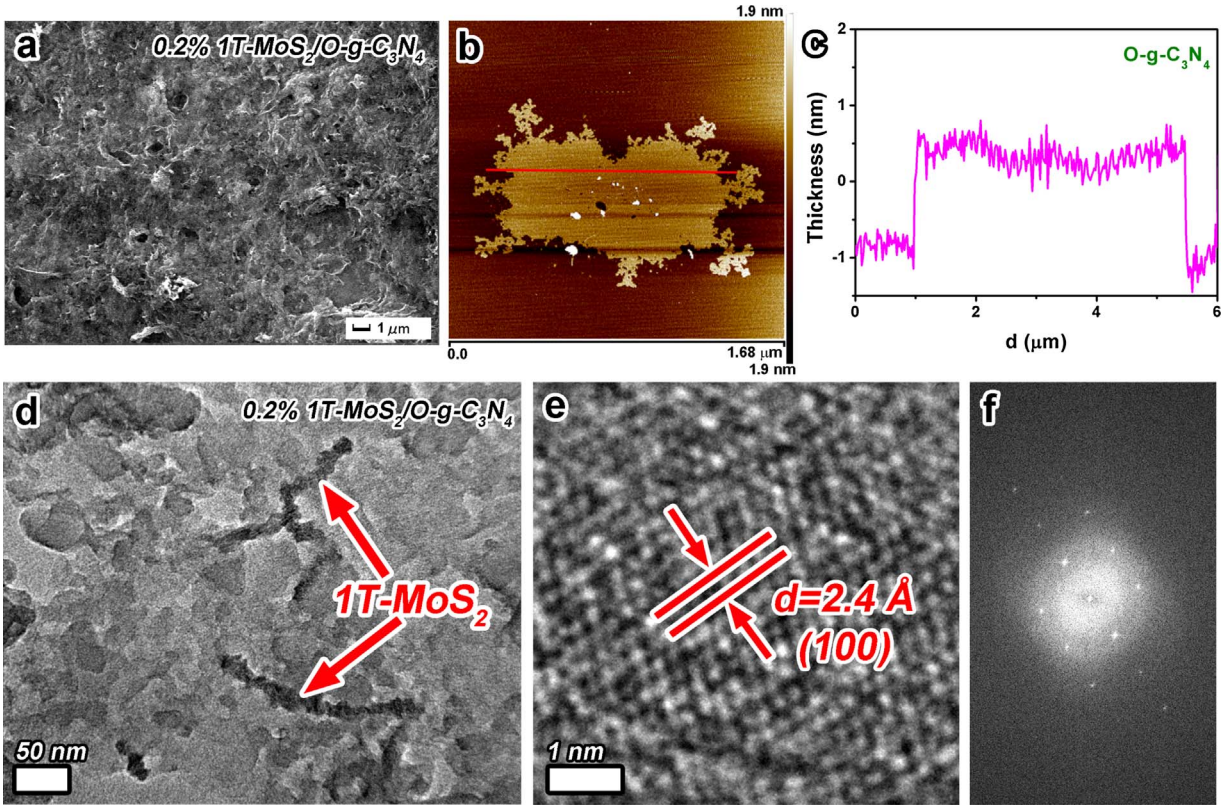

Fig. 2. (a) SEM image of 0.2% 1T-MoS_2/O-g-C_3N_4. (b) AFM image of the pure O-g-C_3N_4. (c) Thickness profile of O-g-C_3N_4 across the red line in (b). (d) TEM image of 1T-MoS_2/O-g-C_3N_4 with loading of 1T-MoS_2 0.2%. (e) High resolution TEM image of 1T-MoS_2. (f) FFT pattern of (e). (For interpretation of the references to colour in this figure legend, the reader is referred to the web version of this article.)

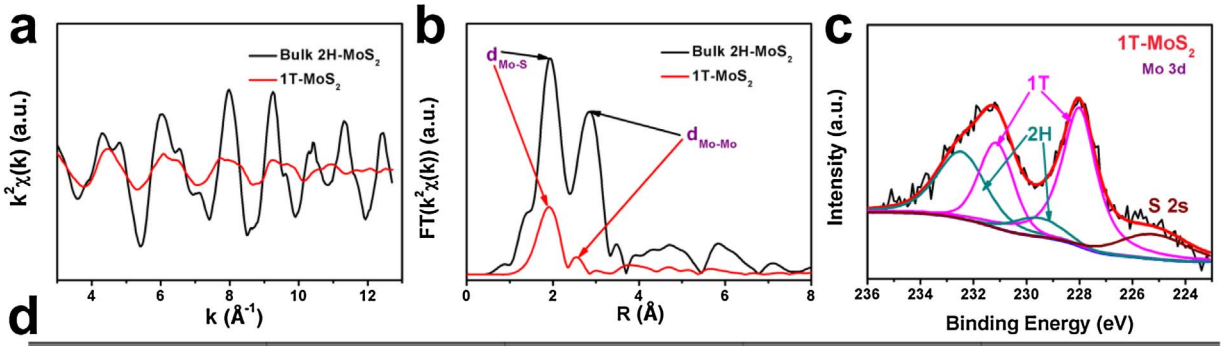

d

Central atoms	Path	Bond length (Å)	*N*	$\sigma^2(10^{-3}$ Å$^2)$
Bulk 2H-MoS_2	Mo-S	2.41	6	3.2
	Mo-Mo	3.17	6	2.7
1T-MoS_2	Mo-S	2.41	2.6	6.9
	Mo-Mo	2.77	1.3	12.0

Fig. 3. (a) Mo *K*-edge oscillation functions $\kappa^{2\chi}(k)$. (b) Corresponding FT analyses revealing the shortening of Mo–Mo bond length and reduced Mo-S coordination number in the 1T-MoS_2 compared to bulk 2H-MoS_2. (c) XPS spectrum of Mo 3d in 1T-MoS_2. (d) Fitted local structural parameters for absorbed Mo in bulk 2H-MoS_2 and 1T-MoS_2 from EXAFS data, indicating a distorted structure of 1T-MoS_2 compared with bulk 2H-MoS_2.

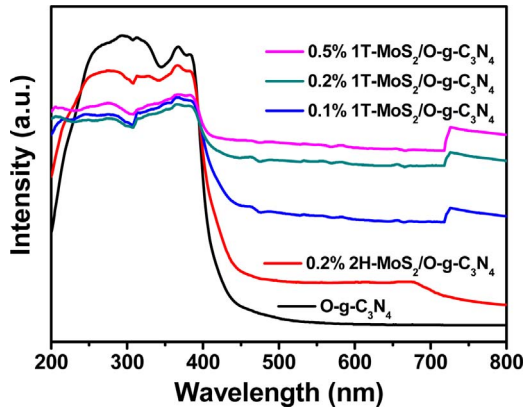

Fig. 4. UV–vis absorption spectra of O-g-C_3N_4, 0.1%, 0.2%, 0.5% 1T-MoS_2/O-g-C_3N_4 and 0.2% 2H-MoS_2/O-g-C_3N_4.

a 400 nm long-wave-pass cut-off filter ($\lambda > 400$ nm). The H_2 evolution was quantified by gas chromatography (GC D7900P, TCD detector).

3. Results and discussion

The in-situ growth route of 1T-MoS_2 on the surface of O-g-C_3N_4 is illustrated in Fig. 1a. In the suspension, Mo^{5+} can self-adsorb onto the surface of the negatively charged O-g-C_3N_4 by electrostatic adsorption (zeta potential of O-g-C_3N_4 is $-10 \sim -25$ mV) [24,25]. Subsequently, Mo^{5+} is reduced by TAA to form MoS_2 on the surface of O-g-C_3N_4 under the high temperature and pressure. Compared with previous assembly of multiple separate materials under low temperature, this in-situ growth ensures the intimate contact between the components, which is beneficial to the separation and transfer of the photo-excited charges.

The as-synthesized MoS_2/O-g-C_3N_4 shows the same X-ray diffraction (XRD) pattern to the pure O-g-C_3N_4 because of ultra-low loading (0.1-0.5%) of MoS_2 (Fig. 1b). Only a peak at ~27.7° corresponding to the interlayer stacking reflection of (002) is obviously observed. The in-plane facet (100) locating at 13.1° disappears attributed to the 2D structure of O-g-C_3N_4 (see AFM results of O-g-C_3N_4 thickness in Fig. 2b-c). The X-ray photoelectron spectroscopy (XPS) survey spectra can detect C, N, O, Mo and S elements, which could indicate the co-existence of O-g-C_3N_4 and MoS_2 (Fig. 1c). The Fourier Transform infrared spectroscopy (FT-IR) spectra confirm the matrix structure of O-g-C_3N_4 in the synthesized MoS_2/O-g-C_3N_4 composite (Fig. S2) [23,26].

The MoS_2/O-g-C_3N_4 material possesses 2D nanosheet morphology that is almost transparent to electron beams and its surface is curled and wrinkled as shown in Transmission Electron Microscope (TEM) and Scanning Electron Microscope (SEM) images (Fig. 2a–d and Fig. **S**3). The Atomic Force Microscope (AFM) shows that the thickness of the pure O-g-C_3N_4 is 1.65 nm close to a single unit cell thickness (Fig. 2b-c). The MoS_2 in nanoribbon structure can be observed in a higher magnification TEM image. A close observation in the High-resolution TEM image, the MoS_2 displays the (100) facet with a 2.4 Å lattice fringe (Fig. 2e). The correspondent fast Fourier transform (FFT) pattern shows a hexagonal symmetry with distortion, consistent with the previously reported 1T-MoS_2 structure (Fig. 2f). We assume the synthesized composite is in the form of 1T-MoS_2/O-g-C_3N_4 2D heterostructure.

In order to further verify the 1T phase of MoS_2 in the synthesized composite, Extended X-ray absorption fine structure (EXAFS) was performed on the composite and the commercial 2H-MoS_2 counterpart. Fig. 3a shows oscillation curves of Mo K-edges of the MoS_2 in the composite and 2H-MoS_2 in the k range of 3.0–12.7 $Å^{-1}$. Obviously, $\kappa^{2\chi}(k)$ of MoS_2 in the composite is very different from that in the 2H-MoS_2. The Fourier transform (FT) profiles in the real space further reveals the difference of bonding length and coordination number in the

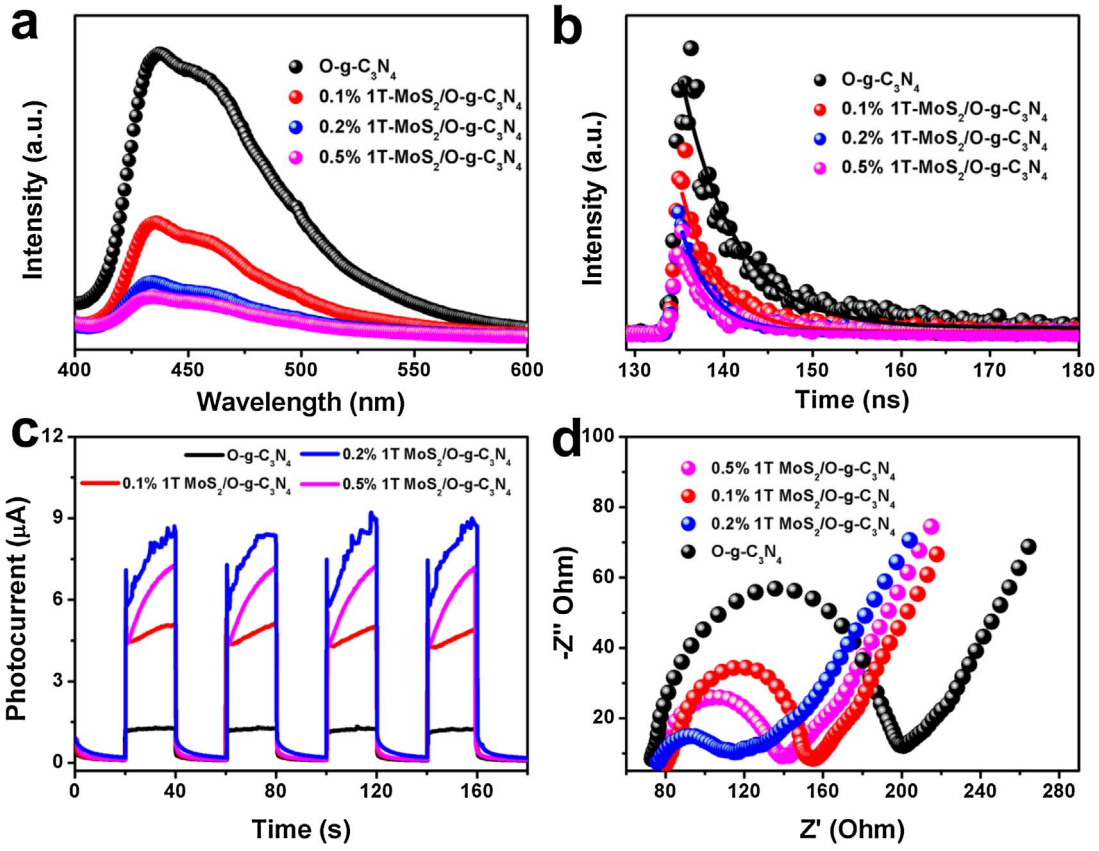

Fig. 5. (a) PL emission spectra of O-g-C_3N_4 and (0.1%, 0.2% and 0.5%) 1T-MoS_2/O-g-C_3N_4 excited at 384 nm. (b) Time-resolved fluorescence excited by the incident light of 337 nm at room temperature. (c) Chopped photocurrent at a bias potential of −0.2 V *vs.* Ag/AgCl under visible light irradiation. (d) EIS Nyquist plots of the electrodes.

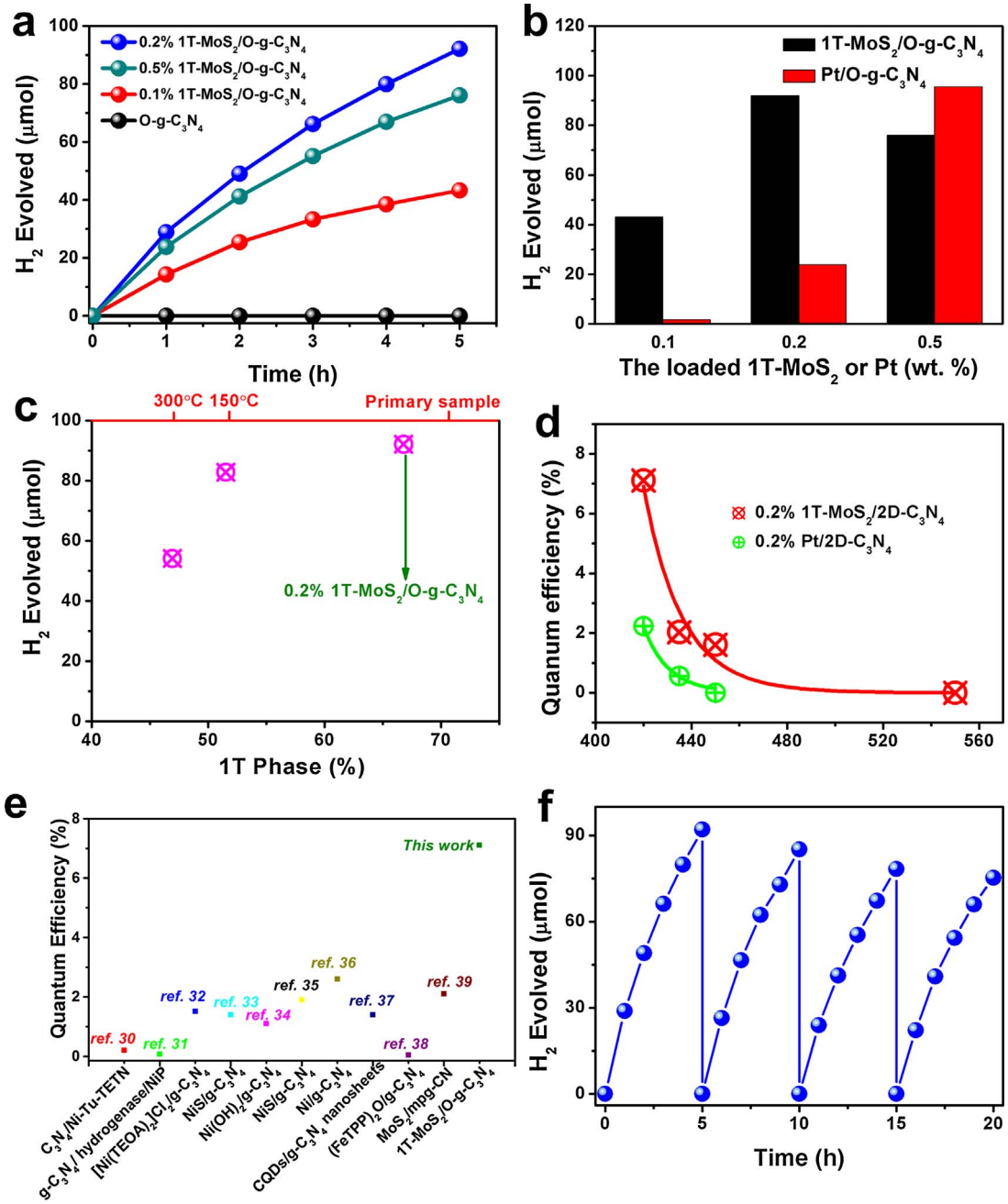

Fig. 6. (a) Photocatalytic H_2 evolution activity of different samples. (b) The H_2 evolution rate in the case of O-g-C_3N_4 loaded with the different content of 1T-MoS_2 or Pt. (c) Photocatalytic activity of the samples as a function of the 1T-MoS_2 concentration prepared by annealing in N_2 atmosphere under different temperatures. (d) Comparison of the quantum efficiency of 0.2% 1T-MoS_2/O-g-C_3N_4 and 0.2% Pt/O-g-C_3N_4. (e) Comparison of the quantum efficiency for the representative g-C_3N_4-based photocatalysts loaded with different non-noble metal co-catalysts. (f) The photocatalytic stability of 0.2% 1T-MoS_2/O-g-C_3N_4.

two MoS_2 species (Fig. 3b). The FT curve of the bulk 2H-MoS_2 owns two main peaks at 3.17 Å and 2.41 Å, corresponding to Mo–Mo and Mo-S bonds, respectively. However, for MoS_2 in the hybrid materials, the second peak for the nearest Mo–Mo bond significantly shifts from 3.17 to 2.77 Å, while the peak at 2.41 Å preserves. The ARTEMIS module was used to analyze the local geometry around Mo. The nearly half coordination number of the Mo–Mo bond referred to six coordination number in 2H phase is a characteristic of the 1T-MoS_2 (Fig. 3d). The high-resolution Mo 3d XPS spectrum of MoS_2 in the composite suggests the predominance of 1T phase (~70% based on the area ratio) over 2H counterpart (Fig. 3**c**). The peaks at ~228.1 and 231.2 eV belong to Mo $3d_{5/2}$ and $3d_{3/2}$ for 1T-MoS_2, respectively. The binding energies of Mo 3d for 1T phase are lower than that for 2H phase (Mo $3d_{5/2}$ ~229.4 and $3d_{3/2}$ 232.5 eV). Additionally, the XPS spectrum of S 2p is consistent with that of 1T-MoS_2 predominance (Fig. S4). Therefore, the assignment of MoS_2 to 1T phase in the composite is reasonable.

The optical properties of the samples were characterized by the UV–vis diffuse reflectance spectroscopy (DRS), time-resolved fluorescence and photoluminescence (PL). In Fig. 4, the absorption edge of pure O-g-C_3N_4 is ~ 450 nm. The absorbance intensity in the whole visible light of the composites gradually increases with increasing 1T-MoS_2 content due to its black color. With the same loading amount, the absorption intensity for 1T-MoS_2/O-g-C_3N_4 is higher than that of 2H-MoS_2/O-g-C_3N_4 in visible light region, which maybe because of the metallic nature of 1T-MoS_2. The intensity of PL can reflect the extent of recombination of the photo-generated charges. In Fig. 5a, it shows that O-g-C_3N_4 possesses a serious charge recombination. When a co-catalyst

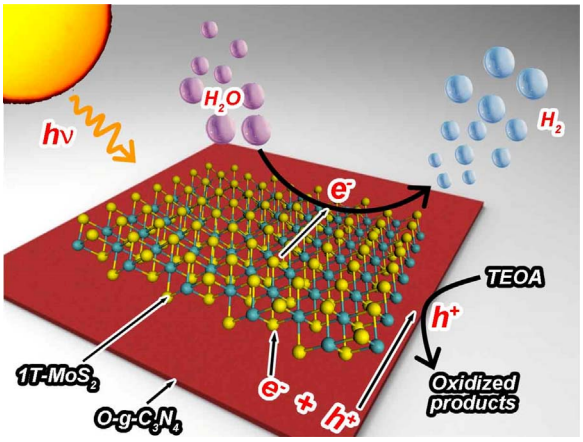

Fig. 7. Scheme illustration of the charge transfer behavior of 1T-MoS_2/O-g-C_3N_4 under visible light irradiation.

1T-MoS_2 is loaded, the PL is drastically quenched (Fig. 5a). Obviously, the recombination of photo-generated e-h pair in O-g-C_3N_4 can be suppressed by transferring electrons to 1T-MoS_2 as the electron acceptor. A faster decay of PL (shorter lifer time) can be observed by incorporating 1T-MoS_2, which is in agreement with the steady-state PL measurement results. For PL decay curves (PL lifetime), as reported in the references, a quick PL decay with a short lifetime demonstrates a low possibility of the photogenerated electron-hole recombination [27,28]. The higher loading of 1T-MoS_2 leads to a lower probability of the recombination of photo-generated e-h pair as suggested by the decease of the PL lifetime from 4.06 ns for 0.1% 1T-MoS_2 to 3.35 ns for 0.5% (Fig. 5b). The suppression of the e-h pair recombination is further confirmed by the enhanced photocurrents after introducing co-catalysts of 1T-MoS_2 compared to bare O-g-C_3N_4 (Fig. 5c). Obviously, the metallic 1T-MoS_2 as a co-catalyst more efficiently accepts photo-generated electrons from O-g-C_3N_4. Among the variety of 1T-MoS_2 loadings, 1T-MoS_2/O-g-C_3N_4 2D heterostructure with 0.2% 1T-MoS_2 shows the optimal photocurrent, indicating 0.2% 1T-MoS_2/O-g-C_3N_4 possesses the best separation efficiency of e-h pairs. The electrochemical impedance spectroscopy (EIS) corroborate the photocurrent results, showing the smallest charge transfer resistance in 0.2% 1T-MoS_2/O-g-C_3N_4 sample (Fig. 5d).

The photocatalytic activity of the composites towards H_2 evolution from water was evaluated under the visible light ($\lambda > 400$ nm) irradiation. The addition of 1T-MoS_2 drastically enhances the hydrogen evolution rate (Fig. 6a). The optimal activity was observed with a loading of 1T-MoS_2 at 0.2%. More 1T-MoS_2 ($\geq$0.5%) covered on the surface of composites could block the absorption of O-g-C_3N_4 and arouse aggregation of 1T-MoS_2, resulting in the decrease of activity. The comparison of photocatalytic activity of different 1T-MoS_2 and Pt contents is shown in Fig. 6b. With the low percent of co-catalyst ($<=$ 0.2%), 1T-MoS_2 shows HER performance superior to Pt. Specifically, with the same co-catalyst loading of 0.2%, 1T-MoS_2/O-g-C_3N_4 2D heterostructure exhibits H_2 evolution rate reaching ~1841.72 μmol/g/h, which is ~4 times higher than that of Pt/O-g-C_3N_4 (480.15 μmol/g/h). 1T-MoS_2 is *meta*-stable which can be transformed into 2H phase through annealing treatment [29]. To investigate the effect of 1T phase versus 2H counterpart on the photocatalytic activity, the 1T-MoS_2/O-g-C_3N_4 sample was annealed at different temperatures to obtain different ratios of 1T/2H. As the annealing temperature increased, the photocatalytic hydrogen production rate decreased sharply (Fig. 6c), while the percent of 1T-MoS_2 in the composites decreases according to the XPS analysis (Fig. S5). Especially when annealed at 300 °C, the percent of 2H-MoS_2 increases to ~60% and the photocatalytic activity is reduced more than the half. It suggests that the semiconducting few-layer 2H-MoS_2 cannnot act well as an electron transport channel and efficient active sites. The HER activity constrained on the edge sites of 2H-MoS_2 also partly contributes to the deterioration of performance.

The external quantum efficiency (EQE) of 0.2% 1T-MoS_2/O-g-C_3N_4 2D heterostructure was achieved at 7.11% at λ = 420 nm (Fig. 6d). The EQE decreased in the long wavelength conditions, and the value is 2.03% and 1.61% at 435 nm and 450 nm, respectively. As a comparison, we also measured EQE of Pt/O-g-C_3N_4 (0.2% Pt loading). In the case of 420 nm light irradiation, the EQE of 0.2% 1T-MoS_2/O-g-C_3N_4 2D heterostructure is almost 3.2 times higher than that of 0.2% Pt/O-g-C_3N_4 (see more results summarized in Table S1). Compared to the reported values, the EQE of 0.2% 1T-MoS_2/O-g-C_3N_4 (7.11% at λ = 420 nm) stands out as the highest among noble-metal-free co-catalysts loaded g-C_3N_4-based photocatalysts (as shown in Table S2). The other noble-metal-free co-catalysts, like $Ni(OH)_2$ and NiS, etc. [30–39], used in g-C_3N_4 system usually have the EQE in the range of 1%-3%, as shown in Fig. 6e and Table S2. The TOF for 0.2% 1T-MoS_2/O-g-C_3N_4 is calculated as 156.6 h^{-1} (as shown in Table S3), which is higher than Pt-g-C_3N_4 materials, excepted for the single atoms Pt [40]. It was also found that the catalyst concentration affected the EQE. When the usage amount of catalysts was 5 mg, 10 mg, 15 mg and 20 mg in 100 mL water, the EQE was 1.44%, 3.88%, 7.11% and 6.78%, respectively (Fig. S6). More catalysts can affect the light absorption and utilization of the material in water, thus affecting the efficiency. Therefore, the optimum amount of catalyst should be used in ~15 mg/100 mL. This result indicates that EQE is related to the catalyst that can actually be used in practice. Regarding the stability, there is a mild degradation in the first three cycles, afterwards it goes steady (as shown in Fig. 6f). In our design, the 1T-MoS_2 can serve as a co-catalyst for the efficient capture of photo-generated electrons and active sites for hydrogen generation. Typically, the O-g-C_3N_4 as semiconductor can generate photoexcited electron-hole pairs under visible light irradiation, and then the electrons could transfer to the 1T-MoS_2 co-catalyst quickly and participate in the photocatalytic reaction to generate hydrogen molecule. On the other hand, the holes would react with sacrificial agent (TEOA) (Fig. 7). The 1T-MoS_2 in this system can not only steer and accelerate the charge transport but provide numerous active sites on the edge sites and basal plane for hydrogen production [17,41,42]. Moreover, we also prepared a pristine g-C_3N_4/1T-MoS_2 photocatalyst system and evaluated the performance, similar enhancement can be achieved like the case of O-g-C_3N_4. (Fig. S7)

4. Conclusions

In summary, high efficient and Pt-alternative 1T-MoS_2 grew on the surface of O-g-C_3N_4. The 0.2% 1T-MoS_2/O-g-C_3N_4 2D heterostructure showed the highest photocatalytic HER efficiency, and the EQE achieved 7.11% at λ = 420 nm 1T-MoS_2 as co-catalyst with high activity is due to the following reasons: (1) both exposed edges and basal plane can be catalytic active sites. (2) Closed contact layer between 1T-MoS_2 and O-g-C_3N_4 is more favorable to transfer photo-generated electrons from CB of O-g-C_3N_4 to the surface of 1T-MoS_2, then the electrons would rapidly participate in photocatalytic HER.

Acknowledgments

This work was supported by National Nature Science Foundation of China (21476097, 21776118), U.S. Air Force BRI Grant (FA9550-14-1-0268) “Science and Emerging Technology of 2D Atomic Layered Materials and Devices”, Six talent peaks project in Jiangsu Province (2014-JNHB-014).

A Project Funded by the Priority Academic Program Development of Jiangsu Higher Education Institutions.

Appendix A. Supplementary data

Supplementary data associated with this article can be found, in the online version, at http://dx.doi.org/10.1016/j.apcatb.2017.08.035.

References

[1] M.G. Kibria, R. Qiao, W. Yang, I. Boukahil, X. Kong, F.A. Chowdhury, M.L. Trudeau, W. Ji, H. Guo, F.J. Himpsel, L. Vayssieres, Z. Mi, Adv. Mater. 28 (2016) 8388–8397.
[2] Y. Zhang, L. Han, C. Wang, W. Wang, T. Ling, J. Yang, C. Dong, F. Lin, X.-W. Du, ACS Catal. 7 (2017) 1470–1477.
[3] T. Oshima, D. Lu, O. Ishitani, K. Maeda, Angew. Chem. Int. Ed. 54 (2015) 2698–2702.
[4] L. Li, Z. Deng, L. Yu, Z. Lin, W. Wang, G. Yang, Nano Energy 27 (2016) 103–113.
[5] S. Bai, L. Yang, C. Wang, Y. Lin, J. Lu, J. Jiang, Y. Xiong, Angew. Chem. Int. Ed. 54 (2015) 14810–14814.
[6] J. Cai, Y. Zhu, D. Liu, M. Meng, Z. Hu, Z. Jiang, ACS Catal. 5 (2015) 1708–1716.
[7] J. Yu, L. Qi, M. Jaroniec, J. Phys. Chem. C 114 (2010) 13118–13125.
[8] K.D. Rasamani, Z. Li, Y. Sun, Nanoscale 8 (2016) 18621–18625.
[9] X. Wang, S. Blechert, M. Antonietti, ACS Catal. 2 (2012) 1596–1606.
[10] W.J. Ong, L.L. Tan, Y.H. Ng, S.T. Yong, S.P. Chai, Chem. Rev. 116 (2016) 7159–7329.
[11] G. Zhang, Z.A. Lan, X. Wang, Angew. Chem. Int. Ed. 55 (2016) 15712–15727.
[12] X. Zhang, Z. Lai, C. Tan, H. Zhang, Angew. Chem. Int. Ed. 55 (2016) 2–25.
[13] G. Li, D. Zhang, Q. Qiao, Y. Yu, D. Peterson, A. Zafar, R. Kumar, S. Curtarolo, F. Hunte, S. Shannon, Y. Zhu, W. Yang, L. Cao, J. Am. Chem. Soc. 138 (2016) 16632–16638.
[14] D. Voiry, H. Yamaguchi, J. Li, R. Silva, D.C. Alves, T. Fujita, M. Chen, T. Asefa, V.B. Shenoy, G. Eda, M. Chhowalla, Nat. Mater. 12 (2013) 850–855.
[15] M. Acerce, D. Voiry, M. Chhowalla, Nat. Nanotechnol. 10 (2015) 313–318.
[16] Q. Liu, Q. Fang, W. Chu, Y. Wan, X. Li, W. Xu, M. Habib, S. Tao, Y. Zhou, D. Liu, T. Xiang, A. Khalil, X. Wu, M. Chhowalla, P.M. Ajayan, L. Song, Chem. Mater. 29 (2017) 4738–4744.
[17] D. Voiry, M. Salehi, R. Silva, T. Fujita, M. Chen, T. Asefa, V.B. Shenoy, G. Eda, M. Chhowalla, Nano Lett. 13 (2013) 6222–6227.
[18] H. Wang, Z. Lu, D. Kong, J. Sun, T.M. Hymel, Y. Cui, ACS Nano 8 (2014) 4940–4947.
[19] R. Raja, P. Sudhagar, A. Devadoss, C. Terashima, L.K. Shrestha, K. Nakata, R. Jayavel, K. Ariga, A. Fujishima, Chem. Commun. 51 (2015) 522–525.
[20] Q. Liu, X. Li, Q. He, A. Khalil, D. Liu, T. Xiang, X. Wu, L. Song, Small 11 (2015) 5556–5564.
[21] R. Kappera, D. Voiry, S.E. Yalcin, B. Branch, G. Gupta, A.D. Mohite, M. Chhowalla, Nat. Mater. 13 (2014) 1128–1134.
[22] Y. Liu, S. Paul, S.-H. Wei, Sci. Adv. 2 (2016) e160069.
[23] X. She, J. Wu, J. Zhong, H. Xu, Y. Yang, R. Vajtai, J. Lou, Y. Liu, D. Du, H. Li, P.M. Ajayan, Nano Energy 27 (2016) 138–146.
[24] F. Cheng, H. Wang, X. Dong, Chem. Commun. 51 (2015) 7176–7179.
[25] S. Cao, J. Jiang, B. Zhu, J. Yu, Phys. Chem. Chem. Phys. 18 (2016) 19457–19463.
[26] X. She, J. Wu, H. Xu, J. Zhong, Y. Wang, Y. Song, K. Nie, Y. Liu, Y. Yang, M.-T.F. Rodrigues, R. Vajtai, J. Lou, D. Du, H. Li, P.M. Ajayan, Adv. Energy Mater. (2017) 1700025.
[27] S. Bai, J. Jiang, Q. Zhang, Y. Xiong, Chem. Soc. Rev. 44 (2015) 2893–2939.
[28] Z. Bian, T. Tachikawa, P. Zhang, M. Fujitsuka, T. Majima, Nat. Commun. 5 (2014) 3038.
[29] K. Chang, X. Hai, H. Pang, H. Zhang, L. Shi, G. Liu, H. Liu, G. Zhao, M. Li, J. Ye, Adv. Mater. 28 (2016) 10033–10041.
[30] D. Wang, Y. Zhang, W. Chen, Chem. Commun. 50 (2014) 1754–1756.
[31] C.A. Caputo, M.A. Gross, V.W. Lau, C. Cavazza, B.V. Lotsch, E. Reisner, Angew. Chem. Int. Ed. 53 (2014) 11538–11542.
[32] J. Dong, M. Wang, X. Li, L. Chen, Y. He, L. Sun, ChemSusChem 5 (2012) 2133–2138.
[33] Y. Lu, D. Chu, M. Zhu, Y. Du, P. Yang, Phys. Chem. Chem. Phys. 17 (2015) 17355–17361.
[34] J. Yu, S. Wang, B. Cheng, Z. Lin, F. Huang, Catal. Sci. Technol. 3 (2013) 1782.
[35] J. Hong, Y. Wang, Y. Wang, W. Zhang, R. Xu, ChemSusChem 6 (2013) 2263–2268.
[36] Y. Chen, B. Lin, W. Yu, Y. Yang, S.M. Bashir, H. Wang, K. Takanabe, H. Idriss, J.M. Basset, Chem. Eur. J. 21 (2015) 10290–10295.
[37] X. Xia, N. Deng, G. Cui, J. Xie, X. Shi, Y. Zhao, Q. Wang, W. Wang, B. Tang, Chem. Commun. 51 (2015) 10899–10902.
[38] D.H. Wang, J.N. Pan, H.H. Li, J.J. Liu, Y.B. Wang, L.T. Kang, J.N. Yao, J. Mater. Chem. A 4 (2016) 290–296.
[39] Y. Hou, A.B. Laursen, J. Zhang, G. Zhang, Y. Zhu, X. Wang, S. Dahl, I. Chorkendorff, Angew. Chem. Int. Ed. 52 (2013) 3621–3625.
[40] X. Li, W. Bi, L. Zhang, S. Tao, W. Chu, Q. Zhang, Y. Luo, C. Wu, Y. Xie, Adv. Mater. 28 (2016) 2427–2431.
[41] S. Bai, L. Wang, X. Chen, J. Du, Y. Xiong, Nano Res. 8 (2014) 175–183.
[42] Q. Liu, Q. Shang, A. Khalil, Q. Fang, S. Chen, Q. He, T. Xiang, D. Liu, Q. Zhang, Y. Luo, L. Song, ChemCatChem 8 (2016) 2614–2619.